The Effects of Sample Position and Gas Flow Pattern on the Sintering of a 7xxx Aluminum Alloy

X.N. YUAN, S.M. AMINOSSADATI, S.H. HUO, G.B. SCHAFFER, and M. QIAN

The effects of sample position and gas flow pattern on the sintering of a 7xxx aluminum alloy Al-7Zn-2.5Mg-1Cu in flowing nitrogen have been investigated both experimentally and numerically. The near-surface pore distribution and sintered density of the samples show a strong dependency on the sample separation distance over the range from 2 mm to 40 mm. The open porosity in each sample increases with increasing separation distance while the closed porosity remains essentially unchanged. A two-dimensional computational fluid dynamics (CFD) model has been developed to analyze the gas flow behavior near the sample surfaces during isothermal sintering. The streamlines, velocity profile, and volume flow rate in the cavity between each two samples are presented as a function of the sample separation distance at a fixed nitrogen flow rate of 6 L/min. The CFD modeling results provide essential details for understanding the near-surface pore distribution and density of the sintered samples. It is proposed that the different gas flow patterns near the sample surfaces result in variations of the oxygen content from the incoming nitrogen flow in the local sintering atmosphere, which affects the self-gettering process of the aluminum compacts during sintering. This leads to the development of different near-surface pore distributions and sintered densities.

DOI: 10.1007/s11661-012-1227-0

I. INTRODUCTION

THE conventional cold-compaction-and-sinter powder metallurgy (PM) process has been employed for the commercial production of near-net-shaped or net-shaped aluminum parts since the early 1970s.[1] Apart from self-lubricating PM Al bearings that require ~20 pct overall porosity[1] and take advantage of open porosity, the pores are not desired in as-sintered Al parts. A special concern is with the near-surface porosity, which decreases the fatigue, wear, and erosion resistance of an as-sintered Al part.[2,3] Islam and Farhat[4] found that the chances of crack nucleation, link-up of pores, and delamination in PM Al-Si alloys increased with increasing near-surface porosity. Grayson *et al.*[5] showed that the onset of fatigue cracks was always associated with a pore or pore cluster situated at or below the surface of an as-sintered 2xxx Al alloy. It is, therefore, necessary to eliminate the near-surface porosity.

However, the factors that dictate porosity including the residual surface and/or near-surface porosity in PM Al parts are not yet clearly understood. In principle, the porosity in a sintered product may result from (1) the primary pores in the green compact, (2) the lubricant after delubrication, (3) the diffusional effect in multi-component alloys (Kirkendall effect), (4) the poor wetting of the liquid with the solid powder surfaces,[6] and (5) vaporization of volatile phases.[7] The near-surface porosity may further be affected by the sintering atmosphere. Experience, including anecdotal evidence from industry, indicates that the gas flow behavior in a sintering furnace, particularly the near sintering surface flow behavior, may play a nontrivial role in the sintering of aluminum alloys. This study aims to identify and characterize the influence of the near-surface gas flow behavior on the surface and/or near-surface porosity through experiments and numerical modeling by computational fluid dynamics (CFD).

CFD modeling has proved to be essential for understanding a variety of fluid flow and heat-transfer-related phenomena in many industrial processes,[8–10] and it has played an important role in the design and optimization of these processes.[11–14] In the context of heat treatment and sintering, however, the use of CFD modeling has been limited. Only a few reports are available where CFD modeling has been used to assist in the understanding of the gas flow behavior in an industrial furnace or incinerator.[15–17] For instance, Saxena *et al.*[18] described a CFD model to predict temperatures of parts in a continuous belt furnace with respect to the belt speeds, part geometry, and loading rates. Stratton and Saxena[19] modeled the effect of the external factors, such as draughts, on the integrity of the furnace atmosphere and the effect of the component parameters on the heating and cooling of the components to optimize the sintering process. No application of CFD modeling to the sintering of metal products has yet been reported.

X.N. YUAN, Ph.D. Candidate, S.M. AMINOSSADATI, Senior Lecturer, and M. QIAN, Reader, are with the School of Mechanical and Mining Engineering, The University of Queensland, CAST-CRC, Brisbane, QLD 4072, Australia. Contact e-mail: ma.qian@uq.edu.au S.H. HUO, formerly Senior Research Fellow, The University of Queensland, is now Vice President, ECKA Granules/SCM Metal Products, Research Triangle Park, NC 27709. G.B. SCHAFFER, Professor, is with the Faculty of Engineering, Architecture and Information Technology, The University of Queensland.

Manuscript submitted August 8, 2011.
Article published online May 30, 2012

PM Al alloys are sintered commercially in nitrogen or nitrogen-rich atmospheres because of the enhanced sintering by nitrogen[20–22] caused by the formation of AlN during the liquid-phase sintering process.[23] This work presents a detailed study of the effect of the gas flow pattern in relation to the sample position on the surface and/or near-surface porosity of a 7xxx aluminum alloy Al-7Zn-2.5Mg-1Cu with the assistance of CFD modeling.

II. EXPERIMENTAL PROCEDURE

A 7xxx aluminum alloy Al-7Zn-2.5Mg-1Cu (wt. pct) was chosen as the model alloy. The powder materials used for fabrication are listed in Table I. Elemental powder mixtures of Al-7Zn-2.5Mg-1Cu were blended in a Turbula powder mixer for 30 minutes with an addition of 1 wt. pct Acrawax C as a lubricant. The powder blends were compacted in a floating uniaxial rectangular die set at 200 MPa using a hand-operated Carver hydraulic press. The compacted rectangular bars measure ~56 mm × 10 mm × 4.5 mm (thickness: 4.5 mm) and weigh approximately 7 g each. The green density (ρ_g) was determined from weight and dimensional measurements, accurate to ±0.0001 g and ±0.001 mm, respectively.

Sintering was conducted in a horizontal stainless steel tube furnace of 160 mm inner diameter. The temperatures were measured by a thermocouple placed approximately 10 mm above the samples. Nitrogen gas with >99.5 pct purity and <100 ppm of oxygen was introduced at a fixed flow rate of Q_{in} = 6 L/min. The dew point of the nitrogen gas was <213 K (–60 °C).[20] Figure 1 shows schematically the dewaxing (40 minutes at 633 K [360 °C]) and sintering processes.

Three samples were sintered in each batch according to the sintering cycle depicted in Figure 1. They were placed perpendicular to the incoming direction of nitrogen and spaced 2 to 40 mm apart. A supplementary sintering test was conducted where three samples were spaced 2 mm apart, heated to 893 K (620 °C) and then removed from the furnace without an isothermal hold. The sintered density was measured using the Archimedes method from oil-impregnated samples. The open porosity was calculated following the method detailed in Reference 24, and the closed porosity was determined by the difference between the total and open porosity.

The theoretical density (ρ_t) was estimated by

$$\rho_t = \frac{1}{\sum_{i=1}^{n} \text{wt pct}_i / \rho_i} \quad [1]$$

where ρ_i is the density of element i in g/cm^3, wt pct$_i$ is the weight percent of element i in the alloy, and n is the total number of element i. The green density (ρ_g) was calculated to be 93.0 ± 0.5 pct theoretical density.

Samples for metallographic examination were cut exactly from the mid cross-section of sintered rectangular bars using a diamond saw. They were ground, polished, and examined in the unetched state using a Polyvar optical microscope (Leica Microsystems GmbH, Wetzlar, Germany).

III. CFD MODELING

The commercial CFD package ANSYS FLUENT 12.0 (ANSYS, Inc., Canonsburg, PA), was used to facilitate the modeling. The geometry considered is a two-dimensional channel with three equally spaced identical samples centered at the base. Figure 2 shows schematically the sintering setup and computational domain. The tubular space measures 2000 mm in length (L) and 160 mm in diameter (D). The samples were placed on a stainless steel plate holder in the hot zone (length l: 300 mm) at ~100 mm (H) below the top of the furnace. Sample 1 is placed at a distance of l_1 from the furnace hot zone inlet and sample 3 is placed at l_3 from the outlet. The working fluid (nitrogen) is introduced into the channel from the inlet at a uniform velocity (u_i) and temperature (T_i), and it is purged from the outlet to simulate the sintering atmosphere. Four different separation distances (d) ranging from 2 mm to 40 mm were set and investigated.

The numerical analysis considered a two-dimensional computational domain (the gray area in Figure 2(a)). This domain included the mid-cross section of each sample. The large size of the computational domain in relation to the sample size ensures that the tubular boundary of the furnace has insignificant impact on the

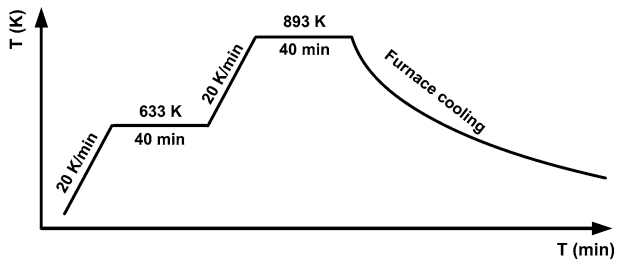

Fig. 1—A schematic diagram showing the dewaxing (633 K [360 °C]) and sintering processes.

Table I. Powder Characteristics

Powder	Source	Grade	Purity (wt pct)	Specified Size (μm)
Al	Ampal Inc. (Palmerton, PA)	650C	99	30 to 300
Zn	Strem Chemicals (Newburyport, MA)	93-3060	99.9	<45
Mg	Alfa Aesar (Ward Hill, MA)		99.6	<45
Cu	U.S. Bronze Powders (Flemington, NJ)	D-101	99.7	<250

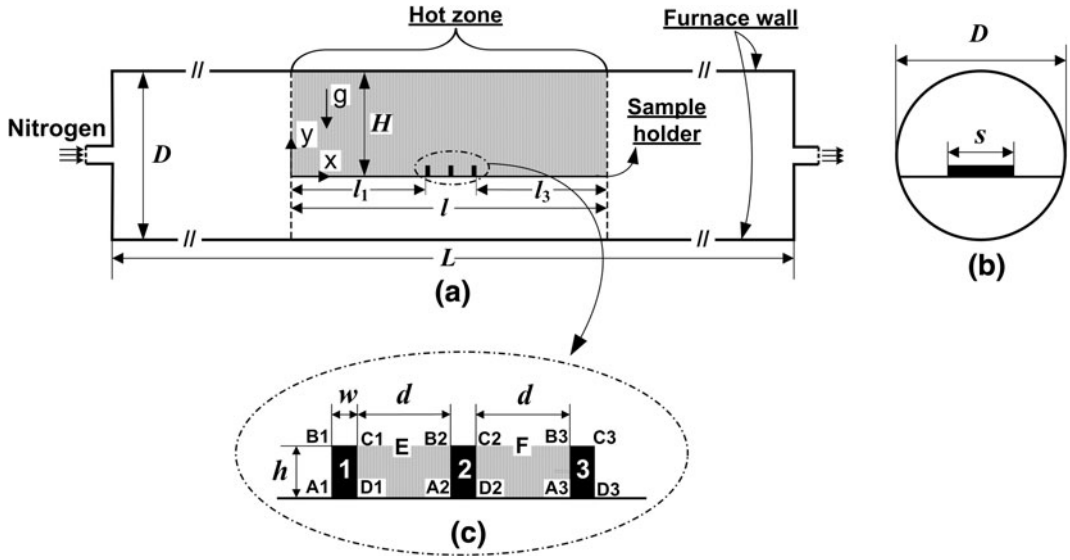

Fig. 2—(*a*) Longitudinal cross section through the furnace and the computational domain (gray), (*b*) diametrical cross section through the furnace, and (*c*) close up view of samples. The samples are labeled as 1, 2, and 3; A*j*, B*j*, C*j*, and D*j* denote the four corners of sample *j*; the two gray regions are referred to as cavity E and cavity F. The samples were placed perpendicular to the incoming gas flow direction.

gas flow reaching the mid-cross section of each sample. This has been confirmed by another CFD study that examined the gas flow entering the spaces between samples from the sides. The results revealed that the gas flow was symmetric to its centerline along the mid-cross section of samples and that the influence of side gas flow on the mid-cross section was negligible. Hence, a two-dimensional computational domain is an acceptable approximation for this study in which the mid-cross section was selected for the pore observation.

A steady-state model was developed for the isothermal sintering process. The underlying assumptions are as follows:

- The nitrogen gas is assumed to be incompressible.
- Given that the variation of the real temperature in the hot zone is minimal during isothermal sintering, the whole modeling domain is assumed to be uniform at the isothermal sintering temperature (T_i = 893 K [620 °C]).
- The properties of pure nitrogen at 893 K (620 °C) are used as input data for calculations, with the density ρ_0 and dynamic viscosity μ being given by 0.3743 kg/m^3 and 3.753 × 10^{-5} Pa.s, respectively.[25]
- The gas flow is laminar because the Reynolds number in the tubular furnace (Re = $\rho_0 u_i D/\mu$) is 8.
- All the samples are assumed to have identical and constant composition, properties, and dimensions through the sintering process (height *h*: 10 mm; width *w*: 4.5 mm).
- The samples are considered to be nonporous because of their high green density (~93 pct theoretical density).

The governing equations of fluid flow satisfying the conservation of mass, *x*-momentum and *y*-momentum can be written in the following nondimensional form:

$$\frac{\partial U}{\partial X}+\frac{\partial V}{\partial Y}=0 \qquad [2]$$

$$U\frac{\partial U}{\partial X}+V\frac{\partial U}{\partial Y}=-\frac{\partial P}{\partial X}+\frac{1}{\mathrm{Re}}\left(\frac{\partial^2 U}{\partial X^2}+\frac{\partial^2 U}{\partial Y^2}\right) \qquad [3]$$

$$U\frac{\partial V}{\partial X}+V\frac{\partial V}{\partial Y}=-\frac{\partial P}{\partial Y}+\frac{1}{\mathrm{Re}}\left(\frac{\partial^2 V}{\partial X^2}+\frac{\partial^2 V}{\partial Y^2}\right) \qquad [4]$$

All the variables and parameters in Eqs. [2] through [4] have been nondimensionalized based on the following definitions:

$$X=\frac{x}{H},\ Y=\frac{y}{H},\ U=\frac{u}{u_i},\ V=\frac{v}{u_i},\ \mathrm{Re}=\frac{\rho_0 u_i D}{\mu},\ P=\frac{pH}{\mu u_i}$$

where D/H = 1.6.

The nitrogen gas is assumed to enter the channel with uniform velocity and the same temperature as furnace wall. The no-slip condition is taken into account on both the upper and lower channel walls and the interfaces between gas and samples. Based on the low Reynolds number (Re = 8) and the length of the computational domain (l = 300 mm), it is expected that the flow has enough downstream space to redevelop. The nondimensional boundary conditions are given as follows:

- At the inlet (X = 0, 0 ≤ Y ≤ 1) U = 1, V = 0
- At the outlet (X = l/H, 0 ≤ Y ≤ 1) $\frac{\partial U}{\partial X}=0$, $V=0$
- Along the channel walls (0 ≤ X ≤ l/H, Y = 0 and 0 ≤ X ≤ l/H, Y = 1) and the interfaces between gas and samples U = 0, V = 0

Figures 3(a) and (b) present a typical, highly variable mesh employed for CFD calculations. Quadrilateral meshes were used, with finer meshes being generated in

the vicinity of each sample. Inflation layers (*i.e.*, those seven layers close to each sample surface and the furnace wall in Figure 3(b)) were applied to the furnace wall and the gas–sample interface to obtain accurate results across the boundary layer and in the sample region. To determine the appropriate grid, a systematic grid independence study was carried out. The ratio of the maximum vertical velocity in the midsection of the cavity between two samples (separated at 40 mm) to the inlet velocity was calculated with respect to five different grid sizes. The results are shown in Figure 3(c). The discrepancy was <2 pct when the grid size was increased from 21,787 to 28,225 cells, hence the selection of 21,787 cells.

The SIMPLE algorithm[26] was applied to solve the pressure-velocity coupling.[27] Convergence was considered

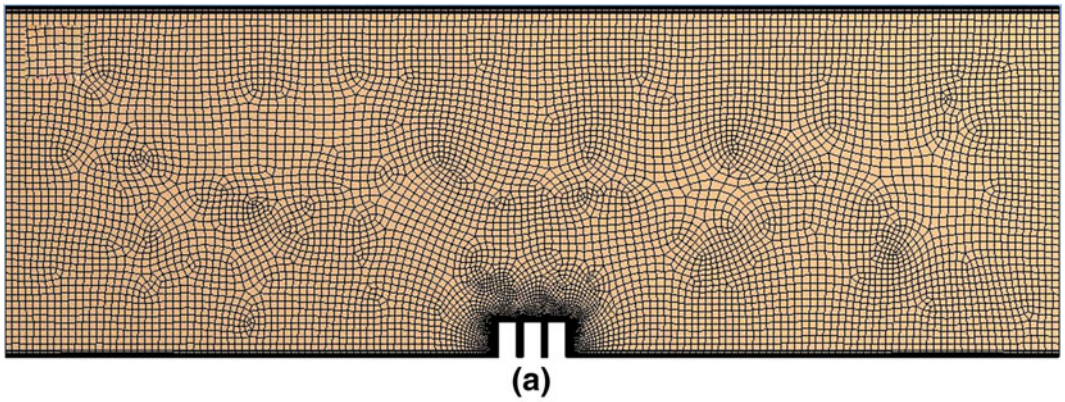

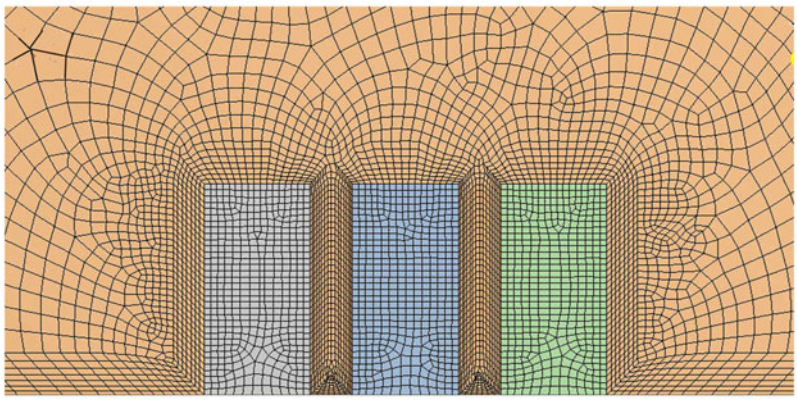

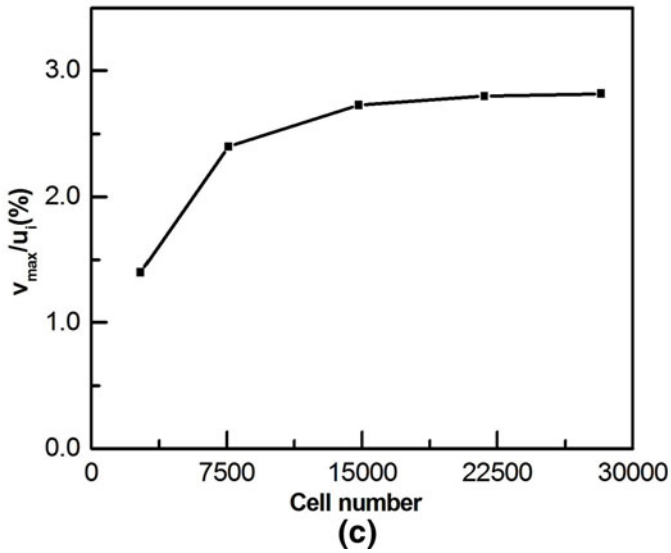

Fig. 3—(*a*) A typical computational domain mesh plot (the mesh within each sample is not shown for clarity). (*b*) A close up of the near-sample region. (*c*) Grid independence study (sample separation distance = 40 mm).

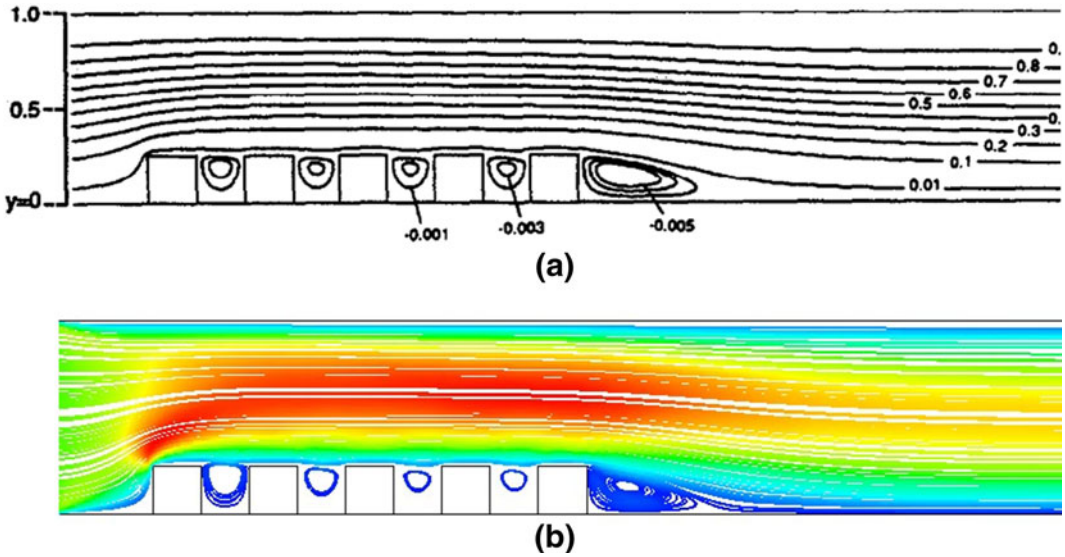

Fig. 4—Validation of the CFD model developed in this study: (*a*) Young and Vafai[11] and (*b*) current work. See Ref. 11 for geometric details. The Re_{D_h} number is equal to 200.

to have been met when the absolute value of residuals was below 10^{-5}.

To validate the CFD approach used, it was assessed against the work by Young and Vafai.[11] Figure 4 shows that the streamlines obtained from the current CFD model are in agreement with the results reported in Reference 11.

IV. EXPERIMENTAL RESULTS

A. *Sintered Density*

Figure 5 shows the density of Al-7Zn-2.5Mg-1Cu alloy sintered at 893 K (620 °C) for 40 min with different separation distances. Despite the discrepancy between the samples sintered in each batch, the sintered density decreases with increasing separation distance. The middle sample, *i.e.,* sample 2, consistently exhibited the highest sintered density when the separation distance is ≤20 mm, whereas sample 1, which faced the furnace inlet, always showed the lowest sintered density. However, the variability decreased with increasing separation distance from 2 mm to 20 mm. At a separation distance of 40 mm, the sintered densities showed a distinctly different pattern and decreased in the sequence of samples 3, 2, and 1.

B. *Pore Distribution*

Figure 6 shows the pore distributions in a cross section of each sample sintered in five batches under different conditions. The following observations are notable:

- The samples that were heated to 893 K (620 °C) and immediately cooled without an isothermal hold had uniform pore distributions (Figure 6(a)). This indicates that the heating and dewaxing stages prior to isothermal sintering had little influence on the difference in the eventual pore distribution. Subsequent work, including the modeling, therefore focused on the isothermal phase.
- The bottom surface of each sample, which was in contact with the supporting tray (stainless steel plate, ~300 × 130 mm), exhibited much less porosity than the corresponding top surface, irrespective of the separation distance.
- When the samples were placed 2 mm apart (Figure 6(b)), the two outermost surfaces were most porous, whereas the inner surfaces between samples showed negligible porosity, except for the presence of a few large pores.
- Increasing the separation distance diminishes the difference between the inner and outer surfaces. The inner surfaces became more porous with increasing the separation distance from 2 mm to 10 mm (Figure 6(c)). At a separation distance of 20 mm (Figure 6(d)), the inner and outer surfaces are similar, whereas at a separation distance of 40 mm (Figure 6(e)), they are essentially the same.

Figure 7 shows the open and closed porosity of the Al-7Zn-2.5Mg-1Cu alloy sintered at different sample separation distances. The open porosity in each sample increases with increasing sample separation distance. In contrast, the closed porosity remains little changed and is essentially independent of the sample separation distance. In addition, in each batch of sintering, the sample that faces the incoming nitrogen gas flow, *i.e.,* sample 1 (Figure 7), always shows the highest open porosity, whereas the middle sample, *i.e.,* sample 2, generally shows the lowest open porosity (samples 2 and 3 show similar open porosity at the separation distance of 40 mm).

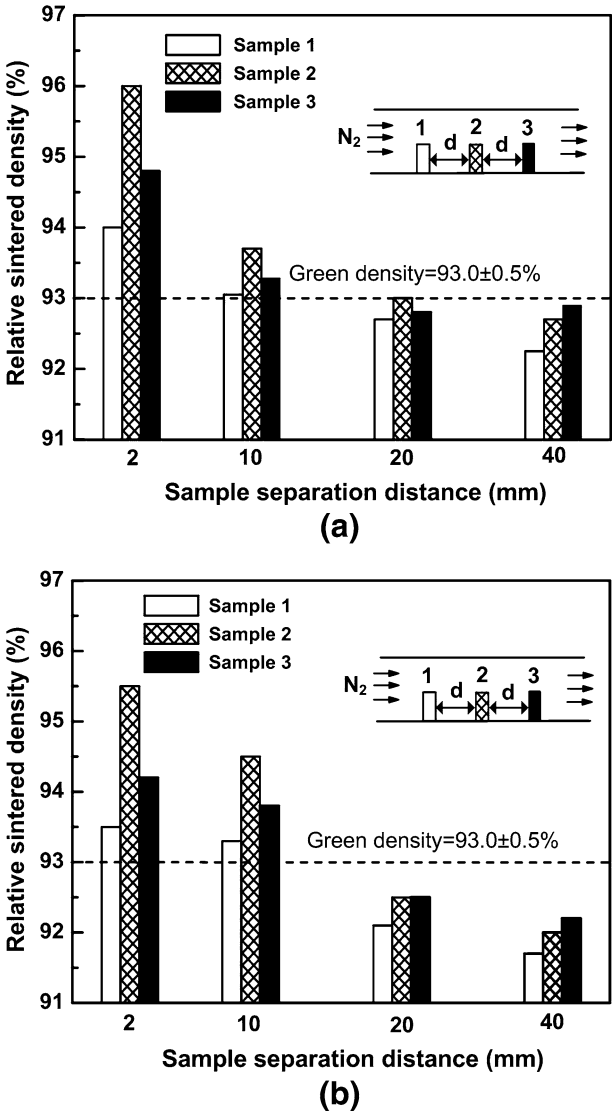

Fig. 5—Densities of Al-7Zn-2.5Mg-1Cu sintered at 893 K (620 °C) for 40 min in nitrogen at a flow rate of 6 L/min. Three samples were sintered in each batch; they were placed perpendicular to the incoming direction of the nitrogen gas and equally spaced from 2 mm to 40 mm apart. The dotted lines show the green density. (*b*) is a repeat of (*a*).

V. CFD MODELING RESULTS

To visualize the flow patterns surrounding each sample, the streamlines were examined.[13,28] Figure 8 presents a close-up of the streamlines in the near-sample region and the velocity profile with respect to different sample separation distances. The normalized vertical component of the velocity profile, the *y*-velocity, corresponds to that at the midsection of each cavity ($y = h/2$). This allows a direct comparison of the gas flow pattern and flow field behavior at the same position in the cavity at different separation distances. Two clockwise recirculation zones are observed for each separation distance, one near the corner of A1 and the other near the corner of D3 (Figure 2 shows the definitions of A1 and D3). The streamlines reveal that the separation distance only affects the flow pattern in the cavity. The details are summarized as follows:

- Figure 8(a) with 2 mm of separation: No streamline develops in each cavity, implying that the gas is essentially stagnant in the cavity during sintering. This finding is supported by the vertical component of the velocity (v/u_i) profile, where $v/u_i = 0$ across the midsection of each cavity (Figure 8(a)). As a result, the gas just flows over the top surface of each sample with no penetration into the cavity between samples.
- Figure 8(b) with 10 mm of separation: The gas flow produces a clockwise circulation in each cavity in addition to the two recirculation zones at the outside of samples 1 and 3. This finding is supported by the sinusoidal *y*-velocity (v/u_i) profile at the midsection of each cavity. The streamlines at the gas–sample interface near the top show gas penetration into each cavity. Consequently, the gas mixed and circulated in each cavity.
- Figure 8(c) with 20 mm of separation: The flow patterns are generally similar to the case when placed 10 mm apart, but several developments are notable. The maximum *y*-velocity becomes greater and gas penetration into the cavity is deeper. The result is a shift of the vortex center toward the bottom of the cavity. In addition, the *y*-velocity profile loses its symmetry, which indicates more extensive gas mixing and circulation in each cavity.
- Figure 8(d) with 40 mm of separation: Noticeable changes have occurred in this case: The gas penetration almost reaches the bottom of each cavity, two independent recirculation zones develop in each cavity, and the maximum *y*-velocity is more than doubled. The gas flow patterns are very similar inside and outside each cavity.

The extent of mixing between the main gas flow and the in-cavity circulation can be further characterized by the volume flow rate through the opening of the cavity. According to the stream function ψ, the volume flow between any two streamlines in a flow field is equal to the change in the stream function between those streamlines[28]:

$$Q_c = \int (\vec{V} \cdot \vec{n}) dA = \int d\psi \qquad [5]$$

The volume flow rate Q_c through the first cavity (cavity E) can thus be calculated from the stream function difference between point C1 and the midpoint of the line segment C1B2 (Figure 2 shows the definition of C1 and B2).

As shown in Figure 8, the difference between the flow patterns in the two cavities is insignificant at all separation distances. Accordingly, the volume flow rate is calculated only for cavity E at each separation distance. The results are plotted in Figure 9 in terms of the volume flow rate ratio (normalized with the inlet volume flow rate) and the oxygen flow into the cavity, calculated according to the oxygen concentration

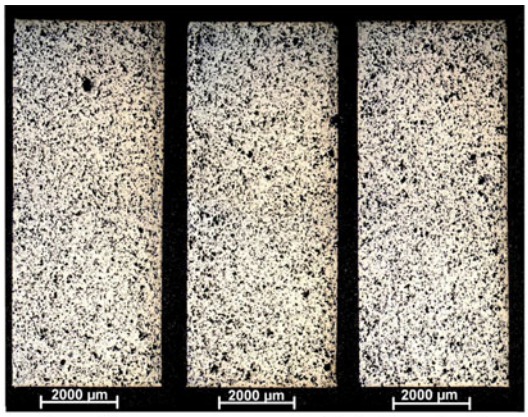

(a) Separation distance: 2 mm, cooled directly from 893 K(620 °C)

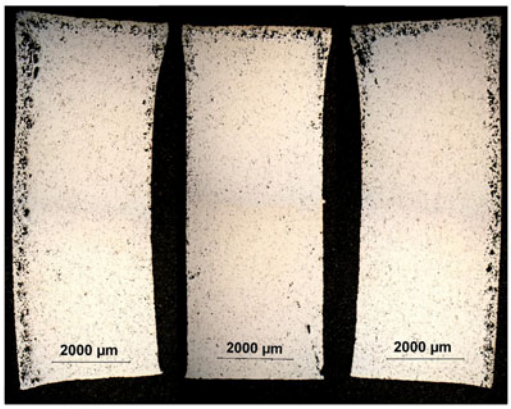

(b) Separation distance: 2 mm

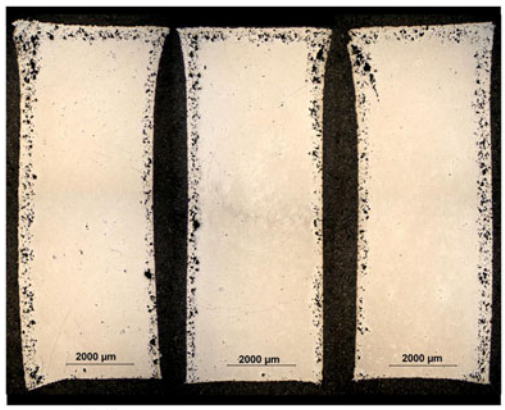

(c) Separation distance: 10 mm

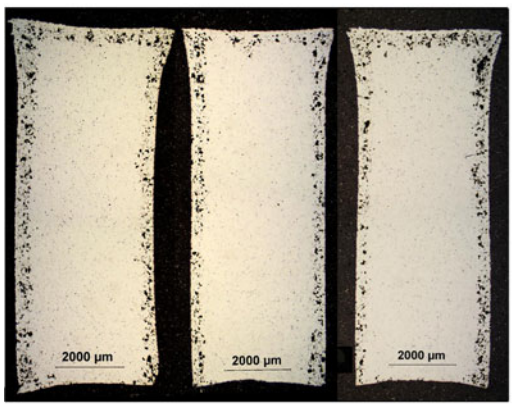

(d) Separation distance: 20 mm

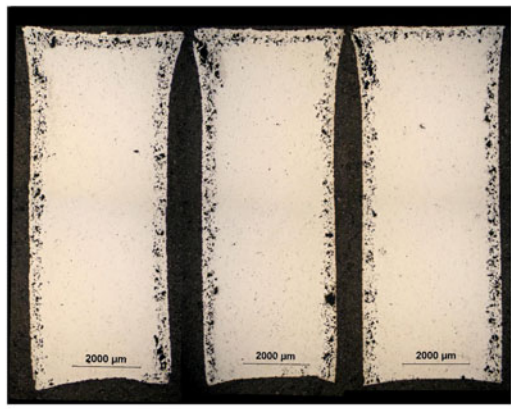

(e) Separation distance: 40 mm

Fig. 6—Pore distributions in samples sintered at four separation distances. The samples in (*a*) were removed from the furnace at 893 K (620 °C) without any isothermal hold. Samples in (*b*) through (*e*) were sintered at 893 K (620 °C) for 40 min.

(100 ppm) in the nitrogen gas used. The volume flow rate through the first cavity (cavity E) is nearly zero at the separation distance of 2 mm, which is consistent with the profiles shown in Figure 8(a). It increases sharply when the separation distance is >10 mm.

VI. DISCUSSION

The CFD modeling results presented provide essential details for understanding the sintered density and near-surface pore distribution with respect to the sample separation distance. The various observations are discussed subsequently based on the CFD modeling results in conjunction with the basic principles established for the sintering of Al alloys.

Because of the high affinity of aluminum for oxygen, each aluminum powder particle is enveloped by an aluminum oxide layer. To enable the sintering of aluminum alloys from powder, this surface oxide layer must be disrupted. However, this would require sintering

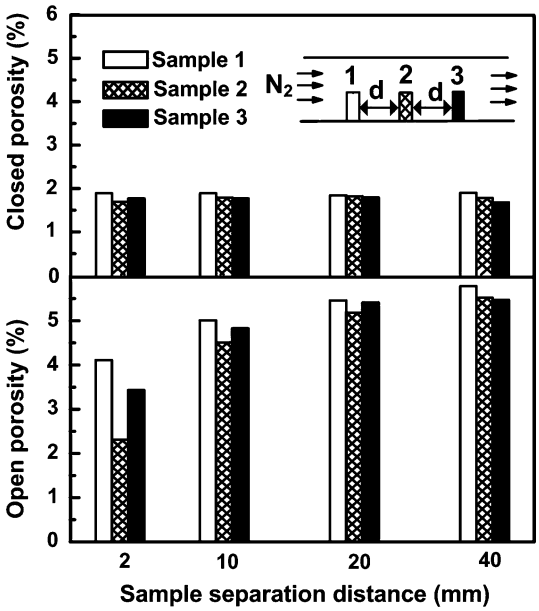

Fig. 7—The open and closed porosity of Al-7Zn-2.5Mg-1Cu alloy sintered at different sample separation distances.

to be done in an atmosphere containing $<2.56 \times 10^{-32}$ Pa of oxygen at the sintering temperature of 893 K (620 °C).[29] Such an extremely low level of oxygen is achievable only through the use of an effective oxygen-gettering agent or the self-gettering by aluminum.[1,29,30] In a porous aluminum powder compact, the outer zone can serve as an effective oxygen self-getter for the inner zone such that the oxygen partial pressure deep in the compact will be essentially zero as the gas penetrates progressively through the pore networks.[29,30] As a consequence, this process often leaves a porous outer zone.

For all cases studied, including the 40-mm separation distance, the vertical surfaces of each sample are shielded from the main flow by a recirculation region. Hence, it is reasonable to assume that the size of that recirculation region and the oxygen diffusion across it will control the oxygen content near the sample surfaces. For instance, the A1B1 and C3D3 surfaces of the samples are exposed to similar recirculation cells. Experimental observations (Figure 6) indicate similar pore densities at the A1B1 and C3D3 surfaces. Similar observations are made with the surfaces of C1D1, A2B2, C2D2, and A3D3 at each separation distance. Increasing the separation distance increases the gas flow into the cavity and, hence, the oxygen content (Figure 9), which leads to increased porosity.

When the samples are placed 2 mm apart, there is virtually no gas penetration from the nitrogen gas flow into each cavity between the samples, as evidenced by the absence of streamlines, close to zero velocity (Figure 8(a)), and near zero flow rate in the cavity (Figure 9). Consequently, the concentration of oxygen in each cavity is maintained at a very low level. This essentially oxygen-free cavity results in effective sintering of the inner surface regions (Figure 6(b)). It is noted from Figure 6(b) that a few pores are still present at the top of each inner surface. This can be attributed to the diffusion of oxygen from the flowing nitrogen near the top surface.

Increasing the separation distance between the samples increases the extent of gas penetration, the velocity magnitude, the gas flow rate, and the degree of gas mixing and circulation in the cavity. Consequently, the difference in the oxygen content between the cavity and the outside is diminished. Each sintering surface is then exposed to an essentially similar sintering environment. For instance, at the separation distance of 40 mm, little difference is predicted for the gas flow patterns inside and outside each cavity (Figure 8(d)). This finding corresponds to the very similar pore distributions between the inner and outer surfaces (Figure 6(e)). As revealed by the observations in Figure 7, increasing the separation distance leads to a consistent increase in the open porosity, which confirms the inferior sintering of the surface as a result of the intensified oxygen attack. The difference in the sintered density at different separation distances (Figure 5) corresponds approximately to the variations of the open porosity.

VII. SUMMARY

The density and near-surface pore distribution of the Al-7Zn-2.5Mg-1Cu alloy sintered in flowing nitrogen (flow rate: 6 L/min) show a strong dependence on the sample separation distance. Few pores are observed on the inner surfaces of the samples at a separation distance of 2 mm during sintering. However, the porosity on the inner surfaces increases dramatically with increasing sample separation distance from 2 mm to 20 mm. When the samples are placed 40 mm apart, both the inner surfaces and the outmost surfaces become similarly porous. CFD modeling reveals that the flow pattern near the sintering surface of each sample is significantly affected by the sample separation distance. The gas in the cavity between each two adjacent samples is essentially stagnant at a separation distance of 2 mm with no penetration from the main gas flow into the cavity. The extent of gas penetration into the cavity increases with increasing sample separation distance leading to increased gas flow rate including the oxygen flow (Figure 9). This occurs particularly when the separation distance is >10 mm at which both in-cavity gas mixing and circulation are predicted. The different gas flow patterns near the sintering surface result in variations of the oxygen content from the incoming nitrogen flow in the local sintering atmosphere, which affects the self-gettering process of the aluminum compacts during sintering. This leads to the development of different near surface pore distributions and, therefore, differences in the sintered density.

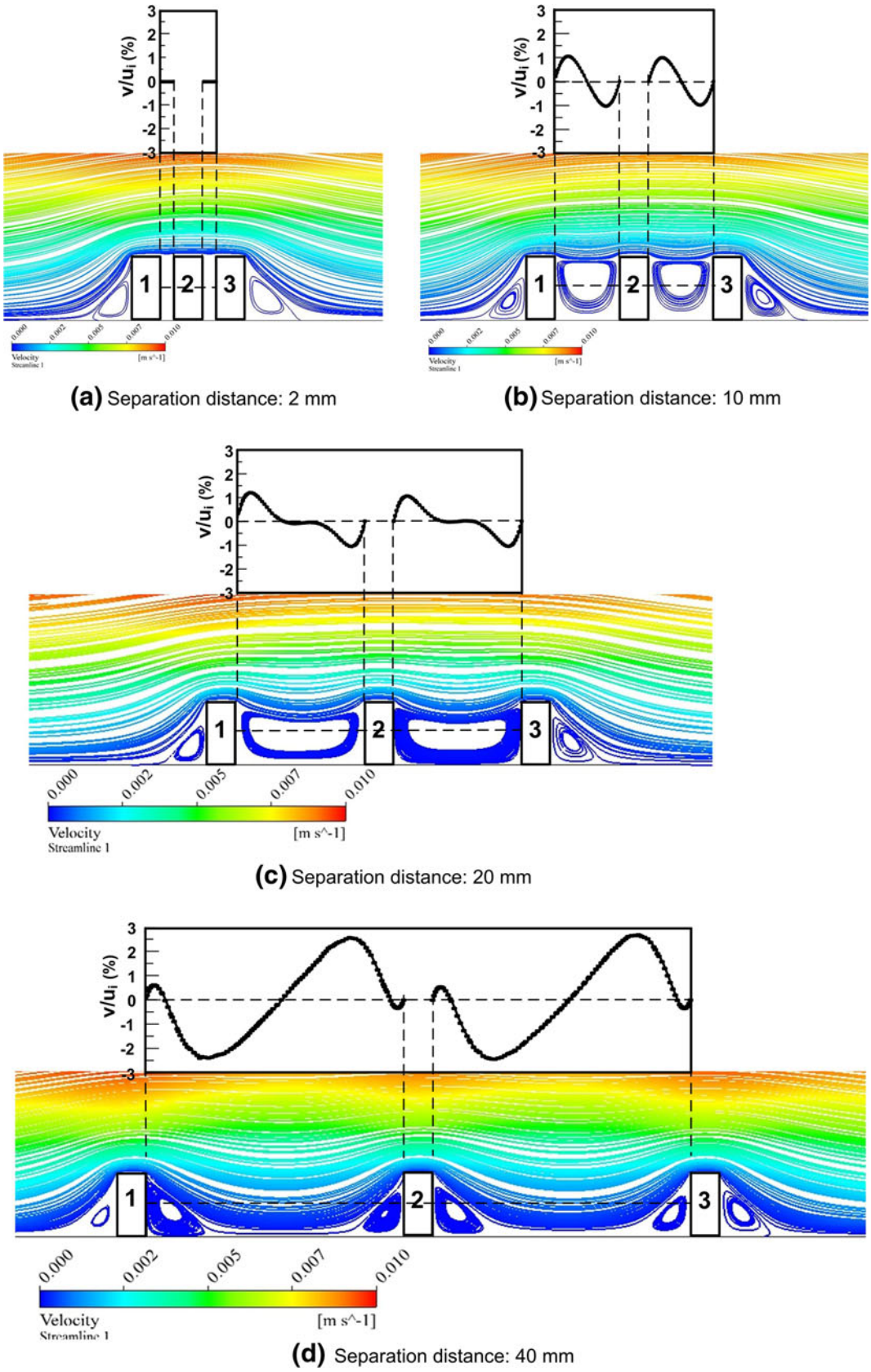

Fig. 8—A close-up of the streamlines in the near-sample regions and the vertical component of the velocity (v/u_i) profile at the midsection of each cavity. The gas flow patterns become essentially similar inside and outside each cavity when the separation distance reaches 40 mm. Significant differences are still noted at the separation distance of 20 mm.

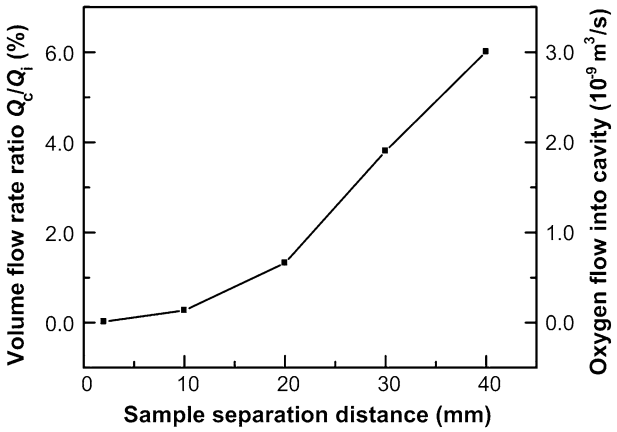

Fig. 9—Volume flow rate ratio and oxygen flow into the first cavity corresponding to different sample separation distances. The oxygen flow was calculated from the gas flow rate and the oxygen concentration (100 ppm) in the nitrogen gas used.

ACKNOWLEDGMENTS

This work was supported by Ampal Inc., a member of the United States Metal Powders Group, through the CAST CRC, a Cooperative Research Center established by the Australian Commonwealth Government. Helpful discussions with Dr. K. Hooman about CFD modeling are gratefully acknowledged. X.N.Y. further acknowledges the support of a CAST-CRC Scholarship and a University of Queensland International Research Tuition Award (UQIRTA). In-depth constructive comments from the Key Reader and reviewer are acknowledged.

NOMENCLATURE

Aj	bottom left corner of sample j
Bj	top left corner of sample j
Cj	top right corner of sample j
Dj	bottom right corner of sample j
D	diameter of the furnace, mm
d	separation distance between two samples, mm
E	cavity between sample 1 and sample 2
F	cavity between sample 2 and sample 3
g	gravitational acceleration, m/s^2
h	height of the sample, mm
H	height of computational domain, mm
L	length of the furnace, mm
l	length of the furnace hot zone (computational domain), mm
l_1	distance from sample 1 to the hot zone (computational domain) inlet, mm
l_3	distance from Sample 3 to the hot zone (computational domain) outlet, mm
n	total number of elemental powders
$\vec{n}$	normal direction to the sample surface
p	pressure, Pa
P	nondimensional pressure
Q_c	nitrogen volume flow rate through the cavity, L/min
Q_i	nitrogen volume flow rate to the computational domain, L/min
Q_{in}	nitrogen volume flow rate to the tubular furnace, L/min
Re	Reynolds number, $= \rho_0 u_i D/\mu$
s	length of samples, mm
T	temperature in sintering cycle, K
t	time in sintering cycle, min
T_i	isothermal sintering temperature, K
U	nondimensional velocity component in X-direction
u_i	inlet gas velocity to the computational domain, mm/s
v	velocity component in y-direction, mm/s
V	nondimensional velocity component in Y-direction
$\vec{V}$	velocity vector, mm/s
w	width of the sample, mm
x	horizontal coordinate distance, mm
X	nondimensional horizontal coordinate distance
y	vertical coordinate distance, mm
Y	nondimensional vertical coordinate distance
ρ_g	green density of the compact, g/cm^3
ρ_i	density of elemental powder i, g/cm^3
ρ_t	theoretical density of the alloy, g/cm^3
ρ_0	density of nitrogen, g/cm^3
μ	dynamic viscosity of nitrogen, Pa.s
ψ	stream function

REFERENCES

1. M. Qian and G.B. Schaffer: *Sintering of Advanced Materials*, Woodhead Publishing Limited, Cambridge, U.K., 2010, pp. 289–322.
2. M. Vardavoulias, C. Jouanny-Tresy, and M. Jeandia: *Wear*, 1993, vol. 165, pp. 141–49.
3. K. Kondoh, J. Umeda, and R. Watanabe: *Mater. Sci. Eng. A*, 2009, vol. 499 (1–2), pp. 440–44.
4. M.A. Islam and Z.N. Farhat: *Trib. Int.*, 2011, vol. 44 (4), pp. 498–504.
5. G.N. Grayson, G.B. Schaffer, and J.R. Griffiths: *Mater. Sci. Eng. A*, 2006, vol. 434 (1–2), pp. 1–6.
6. E. Crossin, J.Y. Yao, and G.B. Schaffer: *Powder Metall.*, 2007, vol. 50, pp. 354–58.
7. R.N. Lumley and G.B. Schaffer: *Scripta Mater.*, 2006, vol. 55, pp. 207–10.
8. T. Norton and D.W. Sun: *Trends Food Sci. Tech.*, 2006, vol. 17 (11), pp. 600–20.
9. P. Verboven, N. Scheerlinck, J. De Baerdemaeker, and B.M. Nicolai: *J. Food Eng.*, 2000, vol. 43 (2), pp. 61–73.
10. A.A. Osma, D. Kocaefe, and Y.S. Kocaefe: *Can. J. Chem.*, 2008, vol. 86 (4), pp. 693–99.
11. T.J. Young and K. Vafai: *Int. J. Heat Mass Trans.*, 1998, vol. 41 (21), pp. 3279–98.
12. M.H. Yang, R.H. Yeh, and J.J. Hwang: *Int. J. Heat Mass. Trans.*, 2010, vol. 53 (4), pp. 760–71.
13. S.M. Aminossadati and K. Hooman: *12th U.S./North American Mine Ventilation Symposium*, Reno, NV, 2008.
14. S.M. Aminossadati and B. Ghasemi: *Eur. J. Mech. B/Fluids*, 2009, vol. 28 (4), pp. 590–98.
15. T. Philips, N. Saxena, H. Nayar, and M. Kirschner: *Adv. Powder Metall. Part. Meter.*, 1994, vol. 7, pp. 143–51.
16. N. Saxena, M. Kirschner, H. Nayar, and T. Philips: *Adv. Powder Metall. Part. Meter.*, 1995, vol. 1 (1), pp. 429–40.
17. J.W. Kang and Y.M. Rong: *J. Mater. Process. Technol.*, 2006, vol. 174 (1–3), pp. 109–14.
18. N. Saxena, J. Dwyer, N. Haring, M, Kirschner, and H. Nayar: *Adv. Powder Metall. Part. Mater.*, 1996, vol. 3, pp. 12.43–12.55.

19. P.F. Stratton and N. Saxena: *The 1st International Automotive Heat Treating Conf.*, Puerto Vallarta, Mexico, 1999.
20. G.B. Schaffer, B.J. Hall, S.J. Bonner, S.H. Huo, and T.B. Sercombe: *Acta Mater.*, 2006, vol. 54 (1), pp. 131–38.
21. T. Pieczonka, T. Schubert, S. Baunack, and B. Kieback: *Mater. Sci. Eng. A*, 2008, vol. 478 (1–2), pp. 251–56.
22. G.B. Schaffer, J.Y. Yao, S.J. Bonner, S.J. Pas, and A.J. Hill: *Acta Mater.*, 2008, vol. 56 (11), pp. 2615–24.
23. M. Yan, P. Yu, G.B. Schaffer, and M. Qian: *Acta Mater.*, 2010, vol. 58 (17), pp. 5667–74.
24. P. Yu, M. Yan, G.B. Schaffer, and M. Qian: *Metall. Mater. Trans. A*, 2011, vol. 42A, pp. 2040–47.
25. F.P. Incropera, D.P. Dewitt, T.L. Bergman, and A.S. Lavine: *Fundamentals of Heat and Mass Transfer*, 6th ed., Wiley, New York, NY, 2007, p. 944.
26. S.V. Patankar: *Numerical Heat Transfer and Fluid Flow*, Hemisphere Publishing Corporation, New York, NY, 1980, pp. 126–31.
27. *Ansys Fluent 12.0 Users' guide*, 2009, pp. 26.11–12.
28. F.M. White: *Fluid Mechanics*, 6th ed., McGraw-Hill, New York, NY, 2008, pp. 40–42, 249–52.
29. G.B. Schaffer and B.J. Hall: *Metall. Mater. Trans. A*, 2002, vol. 33A, pp. 3279–84.
30. T.B. Sercombe and G.B. Schaffer: *Acta Mater.*, 2004, vol. 52 (10), pp. 3019–25.